

# Electron transport in very clean, as-grown suspended carbon nanotubes

JIEN CAO, QIAN WANG AND HONGJIE DAI\*

Department of Chemistry and Laboratory for Advanced Materials, Stanford University, Stanford, California 94305, USA

\*e-mail: hdai@stanford.edu

Published online: 4 September 2005; doi:10.1038/nmat1478

**S**ingle-walled carbon nanotubes have shown a wealth of quantum transport phenomena thus far<sup>1–11</sup>. Defect-free, unperturbed single-walled carbon nanotubes with well behaved or tunable metal contacts are important for probing the intrinsic electrical properties of nanotubes. Meeting these conditions experimentally is non-trivial owing to numerous disorder and randomizing factors. Here we show that  $\sim 1\text{-}\mu\text{m}$ -long fully suspended single-walled carbon nanotubes grown in place between metal contacts afford devices with well defined characteristics over much wider energy ranges than nanotubes pinned on substrates. Various low-temperature transport regimes in true-metallic, small- and large-bandgap semiconducting nanotubes are observed, including quantum states shell-filling, -splitting and -crossing in magnetic fields owing to the Aharonov–Bohm effect. The clean transport data show a correlation between the contact junction resistance and the various transport regimes in single-walled-carbon-nanotube devices. Furthermore, we show that electrical transport data can be used to probe the band structures of nanotubes, including nonlinear band dispersion.

Our suspended nanotube devices consisted of individual single-walled carbon nanotubes (SWNTs) grown<sup>12</sup>, in place across pre-formed tungsten/platinum electrodes over a trench with a local metal gate at the bottom of the trench (Fig. 1a). Device fabrication has been described previously<sup>9,13</sup>. The nanotubes were suspended between platinum contacts (suspended length in the range  $L \sim 0.5\text{--}2\ \mu\text{m}$ , Fig. 1b) in native as-grown forms without receiving any wet chemical treatments.

Owing to their relative abundance, we first focused on small-bandgap (energy  $E_g < 100\ \text{meV}$ ) semiconducting (or quasi-metallic) SWNTs<sup>14</sup>. Device no. 1 (Dev1), which consists of an  $L \sim 500\ \text{nm}$  suspended SWNT, shows conductance  $G \leq 1.5e^2/h$  in the p-channel and slightly lower  $G \leq 1e^2/h$  in the n-channel at a temperature  $T = 0.3\ \text{K}$ , where  $e$  is the electron charge and  $h$  is Planck's constant (Fig. 1c). The p-channel ( $V_g < -2\ \text{V}$ ) shows slow Fabry–Pérot<sup>5</sup>-like humps with four peaks riding on each hump. The gap region shows  $G \sim 0$  and the n-channel shows Coulomb-blockade-like peaks (Fig. 1c). Deep into the n-channel (for  $V_g > \sim 4\ \text{V}$ ), four-peak structures (that is, three short-period peaks in  $G\text{--}V_g$  followed by one of longer period, as marked in Fig. 1c, top axis) are discerned again but

not over any obvious Fabry–Pérot hump. The four-peak structures correspond to 'shell-filling' of longitudinally quantized states in the SWNT<sup>7,10,11</sup>. For each shell with a given wavevector  $k_n = n\pi/L$  ( $n$  is the integer index for the shells), four states are available for electron filling owing to degeneracy of the K and K' sub-bands and spin degeneracy (Fig. 1d).

A striking evolution pattern of the shell-filling structures in an axial magnetic field  $\mathbf{B}$  is observed (Fig. 2). In the p-channel of Dev1, we found that under increasing  $|\mathbf{B}|$ , each shell (the circled region in Fig. 2a at  $B = 0$ ) splits into two groups with each group of two peaks shifting up or down, respectively. At higher  $B$  fields, the two up-moving peaks re-group with two down-moving groups from the neighbouring shell, forming a new four-peak shell structure at  $B \neq 0$  (the circled region away from  $B = 0$  in Fig. 2a). The shell-splitting, -crossing and re-forming give rise to well-behaved zigzag patterns in the  $G\text{--}V_g\text{--}B$  plot. The shell-crossing field is  $V_g$ -dependent (as marked by the dashed line in Fig. 2a) and is roughly linear with  $V_g$ . That is, for energies closer to the band edge, the shells cross at lower  $|\mathbf{B}|$  fields.

In Fig. 3, we show another suspended quasi-metallic SWNT (Dev2, tube length  $L \sim 700\ \text{nm}$ ) with p-channel conductance  $G \leq 1e^2/h$ . The overall characteristics of this suspended SWNT are similar to that of Dev1 with shell-filling structures over a wide range of energy (or  $V_g$ ) and clear shell-crossing zigzag patterns in  $\mathbf{B}$  fields. The shell-crossing is more rapid than Dev1 with several crossings observed in the  $\mathbf{B} = 0\text{--}8\ \text{T}$  field range (shown by a steeper slope of the dashed line in Fig. 3b than in Fig. 2a). As discussed later, the origin of this difference is the larger bandgap of the SWNT in Dev2 than in Dev1.

The electron transport data suggest that the suspended SWNTs with  $L < 1\ \mu\text{m}$  seem 'ideal' with clean transport signatures over wide energy ranges and magnetic fields. No signs of significant defects, disorder or perturbation to the SWNTs are apparent. We observed that  $\sim 70\text{--}80\%$  of suspended SWNT devices with  $L < 1\ \mu\text{m}$  (out of 40–50 quasi-metallic ones) behave this way with well defined current  $I\text{--}V_g$  characteristics over a wide range of  $V_g$ . In contrast, we have measured numerous SWNTs grown by the same chemical-vapour-deposition method on substrates but have never obtained transport data as clean as those for the suspended tubes shown here. It is possible that, for SWNTs lying on a substrate, the substrate–SWNT interaction could mechanically flatten the

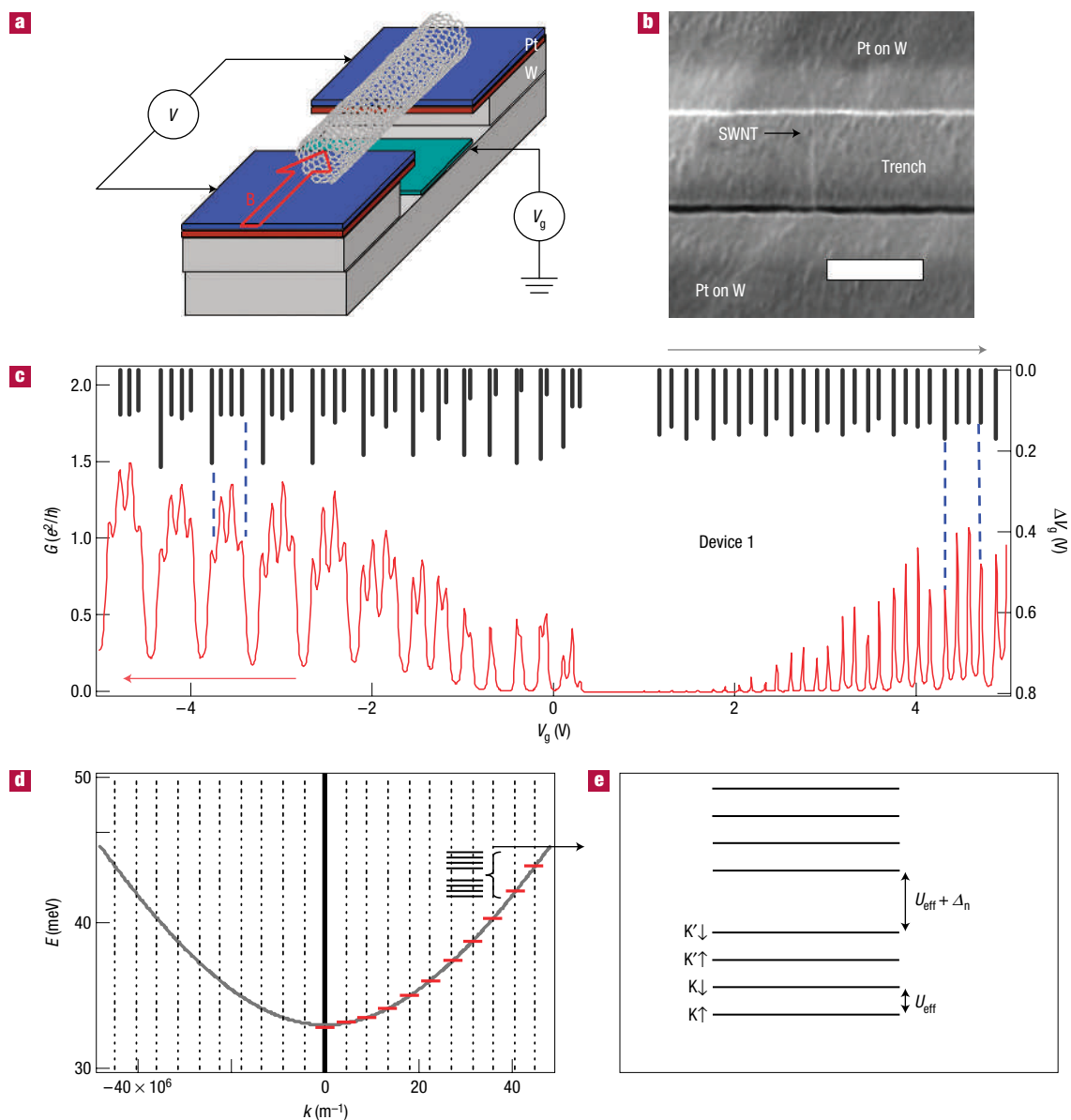


**Figure 1** Suspended SWNTs. **a**, A schematic of the device with a local gate at the bottom of the trench. **b**, A scanning electron microscopy (FEI XL30 Sirion SEM) image of the actual device described in Fig. 3, the scale bar is  $0.5 \mu\text{m}$ . **c**,  $G-V_g$  characteristics of a SWNT (Dev1) recorded at  $T = 300 \text{ mK}$  under  $V = 1 \text{ mV}$  and  $B = 0 \text{ T}$ . The heights of the bars along the top axis correspond to peak spacings  $\Delta V_g$  (right vertical axis) between conductance peaks along the  $V_g$  axis. A four-peak shell is highlighted (by dashed lines) for the p-channel (negative  $V_g$  side) and n-channel (positive  $V_g$  side). **d**, Energy dispersion  $E(k)$  for the valence band. Quantization of wavevectors along the length of the carbon nanotube ( $k_n = n\pi/L$ ) is indicated by evenly spaced vertical lines. Each  $k_n$  gives rise to a shell (represented by the horizontal red levels), each consisting of four states corresponding to the K and  $K'$  sub-bands and spin-up and spin-down. **e**, Details of two of the shells in **c**. Four electrons fill each shell with a charging energy of  $U_{\text{eff}}$ . To reach the next shell, in addition to  $U_{\text{eff}}$ , an energy difference between the quantized shells  $\Delta_n$  needs to be paid.

tube<sup>15</sup>, which could introduce slight perturbation to the nanotube electronic property.

For the four-electron shell structures, we observe similar peak spacings for the four peaks within each shell followed by a larger spacing to the next shell (see the bar heights along the top axes in Figs 1c and 2a). We model the three similar peaks by a parameter  $U_{\text{eff}}$ , which is an effective one-electron addition or charging energy (with exchange sub-band mismatch energy in the model in refs 7,16 included) for four electrons within a shell, and the larger spacing for adding another electron to the next shell (Fig. 1e) by  $U_{\text{eff}} + \Delta_n$ , where  $\Delta_n = E(k_{n+1}) - E(k_n)$ ,  $k_n = n\pi/L$  and  $E(k)$  is the band

dispersion curve (Fig. 2c). Using this simple model, we extract  $U_{\text{eff}}$  from the shell-filling four-peak patterns in  $G-V_g$ . We find that the same nanotube in Dev1 shows  $U_{\text{eff}} = 2.8 \text{ meV}$  in the p-channel with a medium conductance of  $G \sim 1.5e^2/h$  (Fig. 1c, negative  $V_g$  side) and a higher addition energy of  $U_{\text{eff}} = 3.9 \text{ meV}$  in the lower-conductance n-channel (Fig. 1c, positive  $V_g$  side).

The well defined shell-crossing patterns for Dev1 and Dev2 (Figs 2a,3b) reflect the electronic band structures  $E(k)$  of the two nanotubes and  $E(k)$  evolution in magnetic field. Specifically, in zero field, the quantization energy of each shell  $k_n$  relates to the  $E(k)$  dispersion through  $E(k_n) = \hbar v_F \sqrt{(\Delta k_{\perp})^2 + k_n^2}$  in which  $\Delta k_{\perp}$

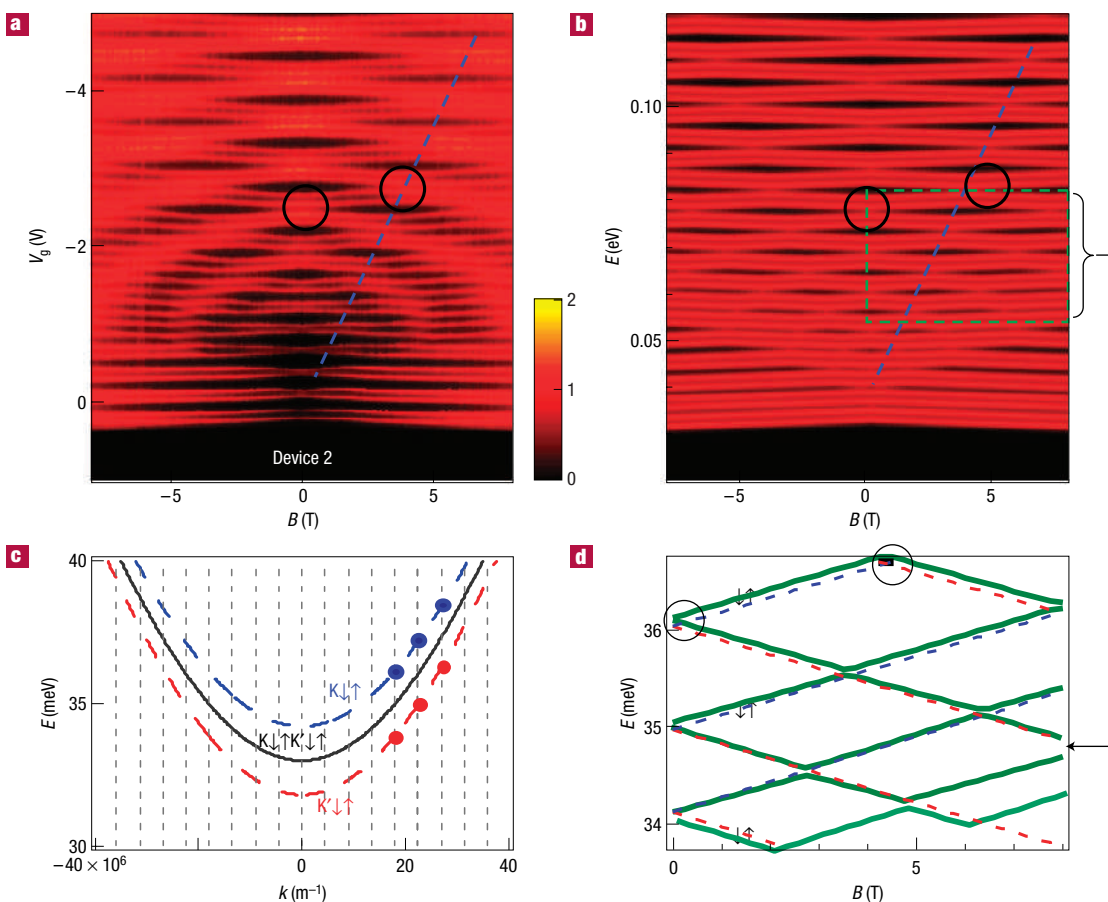


**Figure 2** A suspended quasi-metallic SWNT (the same as Dev1 in Fig. 1) in magnetic fields. **a**, Experimental data of p-channel conductance  $G$  (represented by colour) versus  $V_g$  and  $B$  ( $-8$  to  $8$  T, parallel to the tube axis) based on 160  $G$ - $V_g$  curves from  $B = -8$  to  $8$  T in  $0.1$  T steps. The circles are drawn to highlight two four-peak shells and the one at  $B \sim 5$  T is formed by shell-crossing. The dashed line marks the shell-crossing fields versus energy or  $V_g$ . **b**, The calculated energy  $E$  levels (equation (1)) for the electronic states versus  $B$  and the energy to fit the experimental data in **a**. The region framed by dashed green lines corresponds to Fig. 2d. **c**, Evolution of the K and K' sub-bands in a magnetic field and splitting of shells. **d**, Evolution of the quantized K (red dashed lines) and K' (blue dashed lines) states in each shell as a function of  $B$  according to equation (1) except that the Coulomb charging energy  $U_{\text{eff}}$  is not included. Level crossing occurs as electrons fill in the lower energy states first. This diagram gives rise to the framed region in **b** after including two-fold spin degeneracy and an effective  $U_{\text{eff}}$  between each electron. Note: the gate efficiency conversion factor (between  $V_g$  and  $E$ ) for this device is  $\alpha \sim 0.015$ .

provides a measure of the bandgap ( $E_g = \hbar v_F \Delta k_{\perp}$ ,  $v_F$  is the Fermi velocity in graphene and  $\hbar$  is the reduced Planck constant). Owing to nonlinear  $E(k)$ , the energy spacing  $\Delta_n$  between the quantized shells is energy or  $V_g$  dependent and is small near the bandgap because of flatness of the band there (Fig. 1d). The energy of each state in a certain shell can then be written as  $E_{n,l} = E(k_n) + l \cdot U_{\text{eff}}$ , where  $l = 0, 1, 2, 3$  is the index of the four electrons in each shell. We have

$$E_{n,l} = E(k_n) + l \cdot U_{\text{eff}} = \hbar v_F \sqrt{(\Delta k_{\perp})^2 + \left(\frac{\pi}{L} \cdot n\right)^2} + l \cdot U_{\text{eff}}.$$

The effect of the  $\mathbf{B}$  field can be included by adding the Aharonov–Bohm term<sup>8,9,17,18</sup>

$$\Delta k_{\text{AB}} = \frac{\pi \cdot r}{h/e} B,$$

where  $r$  is tube radius, to give

$$E_{n,l,B} = E_B(k_n) + l \cdot U_{\text{eff}} = \hbar v_F \sqrt{\left(\Delta k_{\perp} \pm \frac{\pi \cdot r}{h/e} B\right)^2 + \left(\frac{\pi}{L} \cdot n\right)^2} + l \cdot U_{\text{eff}}, \quad (1)$$

where the sign ‘+’ is for the K sub-band and the ‘−’ is for the K' sub-band. This gives rise to splitting of the K and K' sub-bands (Fig. 2c) and two up- and down-moving states (the circled states in Fig. 2a), respectively, in each shell.

Without the one-electron addition energy  $U_{\text{eff}}$  in equation (1), the calculated energies of the states in each shell and their evolution in a  $B$  field are shown in Fig. 2d (dashed lines for the K and K' states) with bandgap  $E_g = \hbar v_F \Delta k_{\perp}$  as a fitting parameter. As each electron takes the lowest energy state, a crossing of the states occurs and results in the zigzag pattern of energy levels (the solid lines in Fig. 2d) along the  $\mathbf{B}$  field direction. This is the origin of the shell-crossing pattern observed experimentally. With  $U_{\text{eff}}$  and two-fold spin degeneracy included, we derive the electronic states for all four states in each shell under various  $\mathbf{B}$  fields. By matching the calculated states (Fig. 2b) to those of the experiment (Fig. 2a), including details such as the slopes of the shell-crossing fields, we extract the bandgap  $E_g$  of the SWNT. For the SWNTs in Dev1 (Fig. 2) and Dev2 (Fig. 3), we obtain  $E_g \sim 60$  and  $\sim 100$  meV, respectively.

The physics underlying the more rapid shell-crossing along the field axis for a larger bandgap SWNT (as in Dev2 rather than in

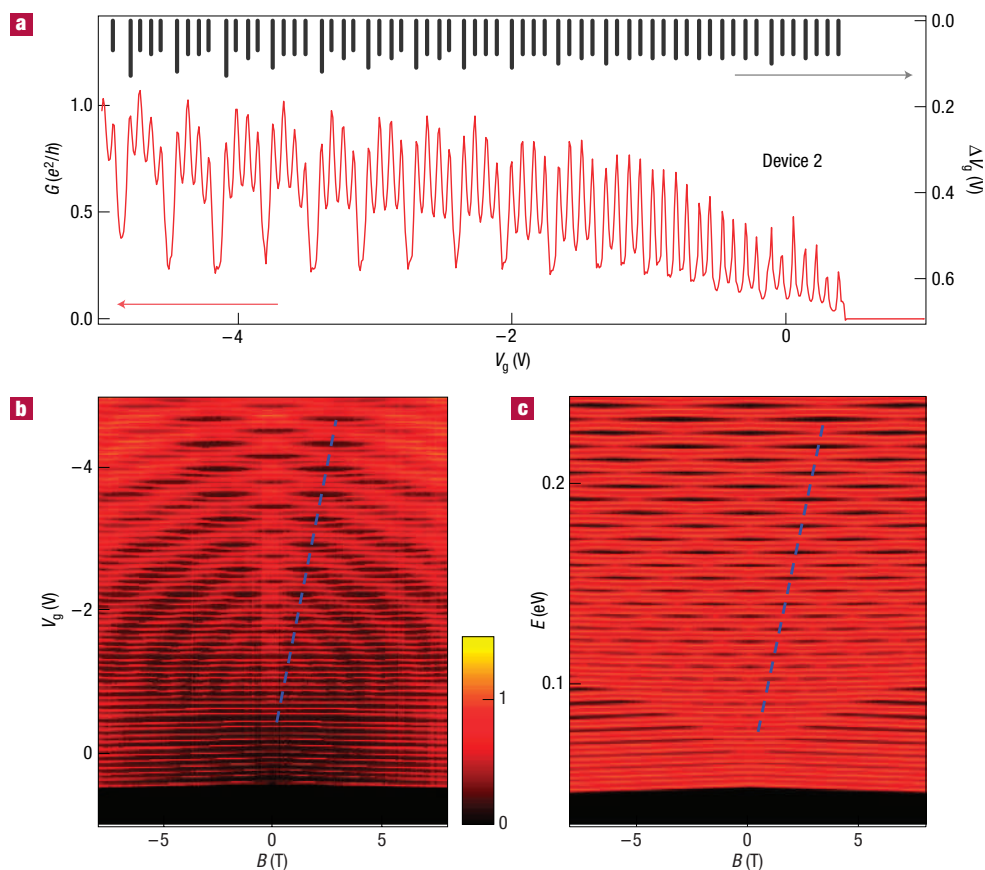


**Figure 3** A second suspended quasi-metallic SWNT (Dev2). **a**,  $G$ - $V_g$  characteristics for the suspended SWNT recorded at  $T = 300$  mK under  $V = 1$  mV. Top: spacing between adjacent conductance peaks. **b**, A plot of  $G$  (represented by colour) versus  $V_g$  and  $B$  ( $-8$  to  $8$  T) based on 160  $G$ - $V_g$  curves from  $B = -8$  to  $8$  T in  $0.1$  T steps. The dashed line marks the shell-crossing fields versus  $V_g$ . The n-channel of this device (not shown) shows a low conductance level and Coulomb blockade. **c**, The calculated energy  $E$  levels for the electronic states versus  $B$  and the energy to fit the experimental data in **b**. Certain discrepancies with the experimental data in **b** are seen near the band edge as the shell-filling model does not apply to states very close to the band edge. Note: the gate efficiency conversion factor (between  $V_g$  and  $E$ ) for this device is  $\alpha \sim 0.032$ .

Dev1) is the flatter  $E(k)$  dispersion for the larger bandgap tube near the band edge. This corresponds to a slower group velocity along the tube axis. The slower-moving electrons accumulate more AB fluxes as they orbit along the tube circumference<sup>8,9</sup>, and therefore experience a greater influence of the magnetic field. The shell-crossing field is energy ( $V_g$ ) dependent (the dashed line in Fig. 2a or 3b) in the same tube as a result of nonlinearity in  $E(k)$  with higher group velocity along the tube axis for states further away from the bandgap. Thus, the electrical transport data show detailed band structures of SWNTs, including bandgap and nonlinearity in  $E(k)$ .

Also interesting is the fact that the high-quality suspended quasi-metallic SWNTs show a systematic trend in conductance level versus SWNT bandgap. In an earlier suspended SWNT with  $E_g \sim 14$  meV and a high conductance of  $G \sim 2.7e^2/h$ , we observed clear Fabry-Pérot interference for p-channel transport<sup>9</sup>. For the two tubes in Dev1 and 2 with larger  $E_g$  (60 and 100 mV, respectively), the p-channel conductance systematically decreases ( $G \sim 1.5e^2/h$  and  $1.1e^2/h$ , respectively). These are attributed to higher and thicker Schottky barriers formed between platinum and the valence band of nanotubes with larger  $E_g$ , and hence higher resistance at the metal-tube junctions owing to a thicker Schottky-barrier width for tunnelling for transport at low temperatures (Fig. 4a). With increasing  $E_g$  and lower  $G$ , the devices show an evolution<sup>19</sup>

from Fabry-Pérot-type interference to shell-filling and then go deep into Coulomb blockade (Fig. 4b). The energy  $U_{\text{eff}}$  increases as the  $G$  level decreases, as seen here for the same nanotube in Dev1 in the p- and n-channels (Fig. 1c) with  $U_{\text{eff}} = 2.8$  and  $3.9$  meV, respectively (owing to larger Schottky-barrier height for the n-channel than for the p-channel with platinum contacts).

We also investigated suspended semiconducting SWNTs with larger bandgaps ( $E_g \sim 0.4$  eV) than the quasi-metallic ones. Devices of this type of SWNT are known to be p-type field-effect transistors at  $T \sim 300$  K with diminished  $G$  under increasing  $V_g$  (Fig. 4c for a  $L \sim 500$   $\mu\text{m}$  suspended tube). At low temperatures, the p-channel  $G$  are typically very low (Fig. 4c,  $G \sim 0.03e^2/h$ , two orders of magnitude lower than at  $T \sim 300$  K) owing to quenched thermal activation over the large Schottky barrier formed at the platinum-SWNT contact junctions (for large  $E_g$ ). Consistent with the trend in Fig. 4b, the p-channels of our suspended semiconducting SWNTs were deep in the Coulomb blockade regime at low temperatures with sharp Coulomb oscillations. Nevertheless, the Coulomb blockade features were highly regular (Fig. 4c), corresponding to a single coherent quantum dot without apparent disorder along the tube length  $L = 560$  nm. Single-dot behaviour has been observed in  $\sim 90\%$  of our suspended-SWNT ( $L < 1$   $\mu\text{m}$ ) devices in the low-conductance limit including  $\sim 30$  semiconducting tubes.

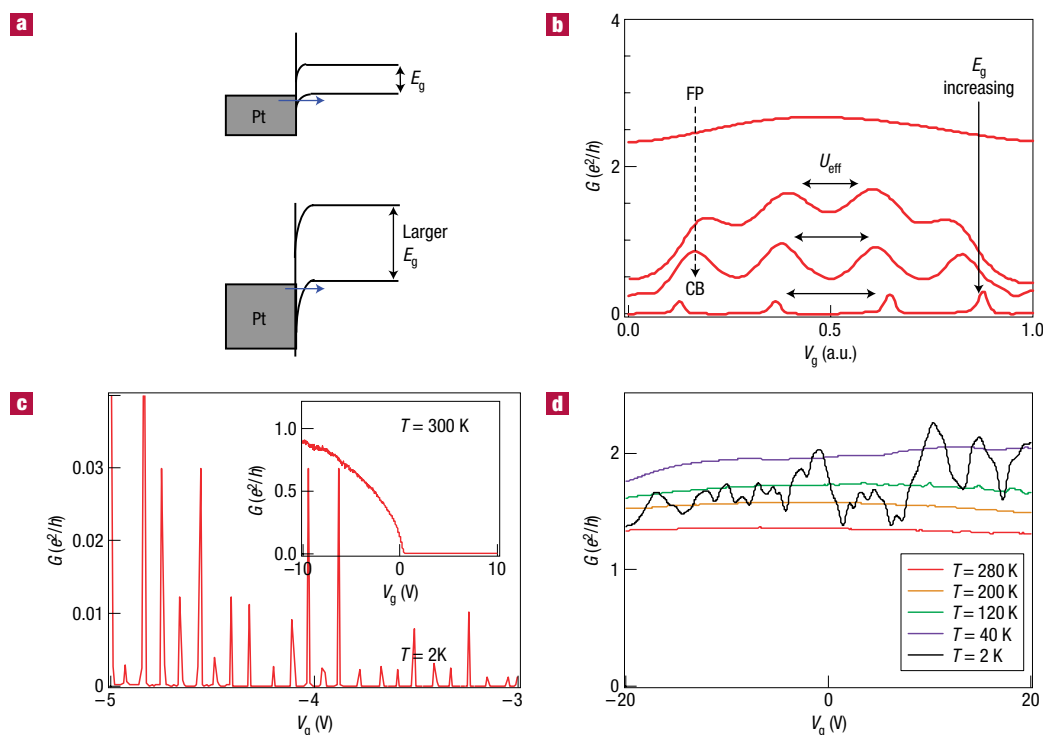


**Figure 4** Contacts and properties of various types of suspended nanotube. **a**, Band diagrams showing a higher Schottky barrier (responsible for higher contact-junction resistance) to the p-channel (valence band) of a larger-bandgap SWNT (bottom panel) than that of a smaller-bandgap tube (top panel) at the metal-tube contact. **b**, A schematic drawing to illustrate the crossover from Fabry-Pérot (FP) interference, to shell-filling (second and third curves, the second one has higher conductance and is over a broad Fabry-Pérot-like peak) and Coulomb blockade (CB) with increasing  $U_{\text{eff}}$  as the conductance level of a nanotube device decreases because of higher contact-junction resistance for larger-bandgap nanotubes contacted by platinum. **c**,  $G$ - $V_g$  characteristics of a suspended semiconducting SWNT at 2 K and room temperature (inset). **d**,  $G$ - $V_g$  characteristics of a true-metallic suspended SWNT at various temperatures.

Finally, we present the electrical characteristics of suspended metallic SWNTs. True-metallic armchair SWNTs are rare with a low abundance of a few per cent<sup>20</sup>. We did encounter one or two such nanotubes out of the  $\sim 100$  suspended devices studied. Figure 4d shows such a suspended metallic SWNT with  $L \sim 2 \mu\text{m}$  showing little gate dependence (over a wide gate-voltage range) from room temperature down to  $T \sim 120 \text{ K}$  accompanied by a metal-like increase in conductance at lower  $T$  (Fig. 4d). Broad oscillation features were observed at  $T = 2 \text{ K}$  over a high-conductance background near  $2e^2/h$ . The lack of gate dependence over a wide temperature range indicates the high quality of the  $2\text{-}\mu\text{m}$ -long suspended tube, as defects and disorders are known to cause energy or gate-dependent resonance transport behaviour for metallic tubes on substrates (at  $300 \text{ K}$ )<sup>21</sup>. We suggest that the as-grown suspended state of metallic SWNT is most likely to preserve the true metallic nature of armchair tubes. However, the irregular Fabry-Pérot-like oscillations observed at  $2 \text{ K}$  (Fig. 4d) do suggest imperfections in the  $2\text{-}\mu\text{m}$ -long suspended tube manifesting in its low- $T$  transport characteristics.

Received 18 February 2005; accepted 29 July 2005; published 4 September 2005.

#### References

1. Tans, S. J. *et al.* Individual single-wall carbon nanotubes as quantum wires. *Nature* **386**, 474–477 (1997).
2. Bockrath, M. *et al.* Single-electron transport in ropes of carbon nanotubes. *Science* **275**, 1922–1925 (1997).
3. Bachtold, A. *et al.* Aharonov-Bohm oscillations in carbon nanotubes. *Nature* **397**, 673–675 (1999).
4. Nygard, J., Cobden, D. H. & Lindelof, P. E. Kondo physics in carbon nanotubes. *Nature* **408**, 342–346 (2000).
5. Liang, W. *et al.* Fabry-Pérot interference in a nanotube electron waveguide. *Nature* **411**, 665–669 (2001).

6. Kong, J. *et al.* Quantum interference and ballistic transmission in nanotube electron wave-guides. *Phys. Rev. Lett.* **87**, 106801 (2001).
7. Liang, W., Bockrath, M. & Park, H. Shell filling and exchange coupling in metallic single-walled carbon nanotubes. *Phys. Rev. Lett.* **88**, 126801 (2002).
8. Minot, E. D., Yaish, Y., Sazonova, V. & McEuen, P. L. Determination of electron orbital magnetic moments in carbon nanotubes. *Nature* **428**, 536–539 (2004).
9. Cao, J., Wang, Q., Rolandi, M. & Dai, H. Aharonov-Bohm interference and beating in single-walled carbon-nanotube interferometers. *Phys. Rev. Lett.* **93**, 216803 (2004).
10. Babic, B., Kontos, T. & Schonenberger, C. Kondo effect in carbon nanotubes at half filling. *Phys. Rev. B* **70**, 235419 (2004).
11. Sapmaz, S. *et al.* Electronic excitation spectrum of metallic carbon nanotubes. *Phys. Rev. B* **71**, 153402 (2005).
12. Kong, J., Soh, H., Cassell, A., Quate, C. F. & Dai, H. Synthesis of individual single-walled carbon nanotubes on patterned silicon wafers. *Nature* **395**, 878–881 (1998).
13. Cao, J., Wang, Q., Wang, D. & Dai, H. J. Suspended carbon nanotube quantum wires with two gates. *Small* **1**, 138–141 (2005).
14. Zhou, C., Kong, J. & Dai, H. Intrinsic electrical properties of single-walled carbon nanotubes with small band gaps. *Phys. Rev. Lett.* **84**, 5604–5607 (2000).
15. Hertel, T., Martel, R. & Avouris, P. Manipulation of individual carbon nanotubes and their interaction with surfaces. *J. Phys. Chem.* **102**, 910–915 (1998).
16. Oreg, Y., Byczuk, K. & Halperin, B. I. Spin configurations of a carbon nanotube in a nonuniform external potential. *Phys. Rev. Lett.* **85**, 365–368 (2000).
17. Ajiki, H. & Ando, T. Electronic states of carbon nanotubes. *J. Phys. Soc. Jpn* **62**, 1255–1266 (1993).
18. Zanic, S. *et al.* Optical signatures of the Aharonov-Bohm phase in single-walled carbon nanotubes. *Science* **304**, 1129–1131 (2004).
19. Alicaia, J., Bena, C., Balents, L. & Fisher, M. P. A. Charge accumulation on a Luttinger liquid. *Phys. Rev. B* **69**, 155332 (2004).
20. Dresselhaus, M. & Dai, H. (eds) *Advances in carbon nanotube. Mater. Res. Soc. Bull.* **29** (special issue), (2004).
21. Bockrath, M. *et al.* Resonant electron scattering by defects in single-walled carbon nanotubes. *Science* **291**, 283–285 (2001).

#### Acknowledgements

This work was supported by MARCO Focused Research Center on Materials, Structures and Devices and a NSF NIRT. Correspondence and requests for materials should be addressed to H.D.

#### Competing financial interests

The authors declare that they have no competing financial interests.

Reprints and permission information is available online at <http://npg.nature.com/reprintsandpermissions/>